Assessing the impact of vortex generators on the dynamic stall behaviour of a thick airfoil

Sahoo, Abhratej; Ferreira, Carlos Simao; Yu, Wei

DOI
10.1088/1742-6596/2767/2/022019

Publication date
2024

Document Version
Final published version

Published in
Journal of Physics: Conference Series

Assessing the impact of vortex generators on the dynamic stall behaviour of a thick airfoil

Journal of Physics: Conference Series **2767** (2024) 022019 doi:10.1088/1742-6596/2767/2/022019

Assessing the impact of vortex generators on the dynamic stall behaviour of a thick airfoil

Abhratej Sahoo[1,2], Carlos Simao Ferreira[2], Wei Yu[2]

[1] TNO Wind Energy, [2] TU Delft Aerospace Engineering

E-mail: abhratej.sahoo@tno.nl

Abstract. Modern slender wind turbine blades use thick inboard airfoils and thicker trailing edges prone to flow separation. The increasing size of these flexible blades amplifies the importance of considering unsteady aerodynamics during the design phase. Environmental conditions result in Leading Edge Erosion (LER), further complicating the sectional unsteady aerodynamic behaviour. Although vortex generators are a well-studied method for passive separation control under steady conditions, their influence on unsteady aerodynamics for clean and rough blade sections is an area that requires further exploration. While some numerical studies exist, reliable experimental data is lacking in the literature. This work presents experimental results on the dynamic stall behaviour of a DU97W300 airfoil, a typical thick root section. The investigation covers both clean and rough conditions, both with and without VGs, to create an understanding of how VGs impact dynamic stall. Moreover, various VG array configurations are used to study the parametric dependence of dynamic stall phenomena on the VG array parameters.

1. Introduction

To meet the growing demands of renewable energy, modern wind turbines are following a trend of increasingly larger rotors [1]. These larger rotors come with slender blades equipped with thick inboard sections prone to flow separation at operating angles of attack [2]. This negatively impacts the turbine's annual energy production, increasing the levelised cost of energy [3]. Passive flow control technologies such as Vortex Generators (VGs) are still preferred over active control due to their simplicity and ability to retrofit standard blades with static add-ons. The impact of VGs in delaying flow separation in airfoils and the flow physics around such airfoil sections are well studied under steady conditions. However, unsteady aerodynamics is playing an increasingly important role in the design of large wind turbines.

Unsteady flow conditions around wind turbine blades can be caused by a variety of reasons, including blade-vortex interactions, yaw misalignment, fluctuating wind direction and shear, and aeroelastic vibrations, to name a few [4–6]. The effect of these unsteady variations of flow around the airfoil surface on the aerodynamic performance can be studied by investigating the effect of time-varying changes in angle of attack. While an airfoil exhibits a fixed angle of attack for leading edge or trailing edge flow separation for steady conditions, unsteady conditions can cause flow to detach and reattach depending on the changes in the flow around the airfoil surface. This cycle of flow separation and reattachment is referred to as dynamic stall. Dynamic stall produces higher unsteady loads on the blade, increasing the chances of fatigue failure and reducing turbine lifetime. Moreover, dynamic stall in some cases also induces negative aerodynamic damping that can cause uncontrolled growth of structural vibrations leading to rapid failure [7, 8].

In addition to surrounding flow conditions, Leading Edge Roughness (LER) on the blades is also one of the leading reasons for the earlier onset of stall in wind turbines. Reduction of AEP can range from about 3.7% to 25% in worst case scenarios, depending on operating conditions and roughness levels [9, 10]. LER causes the flow around affected airfoil sections to prematurely transition to a turbulent boundary layer. In addition to the earlier transition, roughness also changes the nature of the turbulent boundary layer, increasing skin friction. Thus, particularly vulnerable to the effects of LER are inboard sections, whose thickness and camber are responsible for earlier onset of stall and large reduction in lift under rough conditions.
The effectiveness of VGs to delay flow separation and, subsequently, increase AEP has been widely studied [11–13]. VGs have also been shown to be effective in reducing the detrimental effects of leading edge roughness [14, 15]. Conventionally designed as protruding vanes from the blade surface and placed angled with respect to the incoming flow, the primary effect of VGs is to generate streamwise vortices that enhance mixing in the boundary layer. Several parameters influence the production and evolution of these vortices in the boundary layer, and consequently the delay of flow separation [16–18]. While the use of VGs to delay static stall has been widely studied, very few studies exist on the effect of VGs on dynamic stall phenomena. Most existing research has chosen to study VGs and dynamic stall numerically due to the ease of simulating dynamic conditions with modern CFD tools [19, 20]. There are even fewer experimental studies that cover both large Reynolds numbers and high degrees of unsteadiness [21, 22].
This paper aims to address this gap through a comprehensive experimental test campaign spanning airfoils with and without leading edge roughness, VGs, and unsteady motion simulating dynamic stall. The experiments also cover both low and high Reynolds numbers, as well as low and high Strouhal numbers, thus covering a wide range of unsteadiness of the flow.

2. Experiment description

2.1. Model and wind tunnel description

The tests were carried out in the closed-loop, low-turbulence tunnel at TU Delft. The octagonal test section has a cross-sectional area of 1.80 m $\times$ 1.25 m and is 2.60 m long. The airfoil tested is a DU97W300 section with a maximum thickness-to-chord ratio of 30%. The airfoil is designed for the inboard sections of wind turbines with a thick trailing edge for structural stability and a relatively high maximum lift under clean conditions [23]. The maximum C_l of the airfoil drops by a little more than 25% under rough conditions (simulated through zigzag tape at the leading edge), which is acceptable for a thick inboard airfoil. This behaviour is also the reason why this airfoil is a perfect base to study the effectiveness of passive add-ons like VGs that help counter the effects of roughness, among other things. The model has a chord of 0.65 m, a thick trailing edge of 1.7% of the chord, and spans the height of the test section. This gives an aspect ratio of approximately 1.92. The effects of leading edge roughness were created by using zigzag tape of 0.205 mm thickness to force transition to a turbulent boundary layer at 5% chord-wise location on both sides of the airfoil. Throughout the paper, “clean” and “rough” are used to refer to the free or forced transition state of the boundary layer.
The pitching motion for the dynamic stall tests was imparted using a linear actuator connected to a steel shaft going through the model. A crank mechanism converted the linear actuation to the rotational motion of the airfoil. The model was clamped at the top and bottom with rotational bearings, leaving a gap of about 1 mm between the model and the tunnel walls. During static tests, this gap was taped off.
The experiment setup also included a traversable stereoscopic Particle Image Velocimetry (PIV) setup for flow visualisation of the airfoil boundary layer. Due to the page limit, the flow visualisation results will not be included in this paper, and thus the PIV setup is not described here. Nevertheless, the full experiment setup, including PIV equipment, is shown in Figure 1.

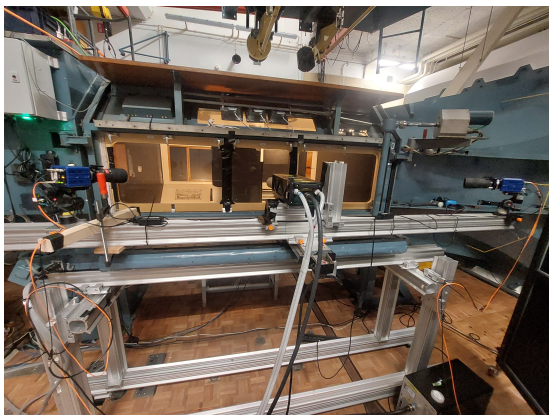

Figure 1: Full experiment setup

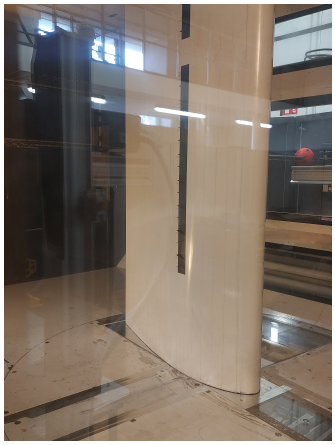

Figure 2: Airfoil model with VG strips

2.2. Vortex Generator design

A VG array placed on a blade section has several key parameters defining it, categorised into either the (a) vane geometry or (b) array configuration parameters. The symbols used for each parameter from now on in the paper are shown in Figure 3a. Based on previous tests [16], a baseline of counter-rotating vanes with a common downwash was chosen as the most optimal array type. The placement of the array was also fixed to 30% chord-wise location on the suction side, as previously determined to be the optimal chord-wise placement of VGs for this airfoil. The VGs were added across the span of the airfoil model, but leaving some gaps near the pressure ports and the walls. A gap of around 35 mm around each side of the pressure ports was left to avoid blocking the nearest pressure ports and to avoid causing fluctuations at the nearest pressure ports due to the VG array mounting strip. There was also a gap of around 100 mm near the top and bottom of the tunnel walls to avoid interactions between the VGs and the flow near the walls. To verify whether these gaps were reasonable, some tests from literature [16] were reproduced. The reproduced tests showed a difference of within 1° in the stall angle of attack with previous tests and thus the effect of the gaps was considered negligible in the overall effect of the VGs. Primarily, triangular vanes were chosen as the most common type of VGs seen in the literature for wind energy applications.

Literature suggests that the height of the VG vanes is the strongest influencing parameter on the strength of the shed vortex and the effectiveness of stall delay [24, 25]. Thus, the vane size was chosen as the primary parameter to vary in the current tests, while the array configuration parameters were secondary. Additionally, for the sake of comparison, all the spacing parameters of the designed VG arrays are expressed and scaled in terms of the vane height. Three different vane sizes with appropriately scaled array configuration parameters were chosen to study the influence on vortex effectiveness. The vane size was kept constant to the largest size tested to study the effect of the secondary array configuration parameters. In addition to the size and placement, the effect of vane shape was also studied by comparing the baseline triangular vane to a rectangular vane. All parameters of the VGs used in this campaign are summarised in Table 1. The VG arrays were manufactured via 3D printing. For ease of manufacture and mounting on the airfoil model, a thin mounting strip of 280 mm length and 0.5 mm thickness was included in the VG array designs, as shown in Figure 3b. The height of the VGs was accordingly adjusted to match the total heights mentioned in Table 1.

(a) Parameter nomenclature (b) CAD model with mounting strip for 3D printing.

Figure 3: VG arrays used in the wind tunnel tests.

Table 1: Summary of VG array geometries tested

VG ID	Vane Shape	β [deg]	L [mm]	h [mm]	D [mm]	d [mm]	Varying Parameter
3	Tri	15	30	10	70	35	Baseline
1	Tri	15	15	5	35	17.5	Vane size
2	Tri	15	7.5	2.5	17.5	8.75	
4	Rect	15	30	10	70	35	Vane shape
5	Tri	15	30	10	70	17.5	Vane spacing
6	Tri	20	30	10	70	35	Inclination Angle

2.3. Test matrix

The test cases are summarised in Table 2. The airfoil was tested with and without ZZ tape, and with and without VGs. The static polars were acquired between $-25°$ and $40°$, capturing the stall region even with VGs. The chord-wise Reynolds numbers were between 0.5 million and 2 million, corresponding to wind speeds between 11.3 m/s to 45.3 m/s. The free-stream turbulence level was thus well below 0.05%.

For the dynamic stall tests, the pitching motion imparted followed an angle of attack sinusoidally varying with time. Sinusoidal pitch oscillations have been found in the literature to represent the effect of dynamic stall phenomena on rotating blades due to yaw and wind shear [26]. For a mean angle of α_0, an amplitude of A, and a frequency of f, the variation of the angle of attack with time t, in seconds, is given by Equation (1).

$$\alpha(t) = \alpha_0 + A\sin(2\pi f t) \tag{1}$$

The mean angles chosen were $5°$ and $10°$. Combined with amplitudes $A = 5°$ to $15°$, the pitching airfoil enters and exits various stages of attached and separated flow, as observed from the steady polars. The frequency varied from $f = 1Hz$ to $3Hz$. The Reynolds numbers chosen were the lowest and highest values of 0.5 million and 2 million. These frequency and Reynolds numbers combinations ensured the airfoil was tested in different unsteady regimes based on the dimensionless reduced frequency k, defined in Equation (2). For the higher Reynolds number (i.e., higher inflow wind speed), $k < 0.05$ corresponded to a flow regime of quasi-steady to light unsteadiness. Whereas, for the lower Reynolds number (i.e. lower inflow wind speed), $k > 0.05$ corresponded to a flow regime of high unsteadiness.

$$k = \frac{\pi c f}{U_\infty} \tag{2}$$

Table 2: Overview of all the test cases

Reynolds Number Re (×1E6) [-]	Transition -	VG Array -	Mean AoA α [°]	Amplitude A [°]	Frequency f [Hz]	Reduced Frequency k [-]
Steady Polars						
0.5, 0.75, 1.0, 2.0, 3.0	clean	-	-25 to 40	0	0	0
0.5, 0.75, 1.0, 2.0, 3.0	rough	-	-25 to 40	0	0	0
0.5, 1.0, 2.0	rough	VG1, VG2, VG3, VG4, VG5, VG6	-25 to 40	0	0	0
Unsteady Polars						
0.5	clean	-	5	5, 10, 14	1, 2, 3	0.1805, 0.3609, 0.4511
0.5	clean	-	10	5, 10, 14	1, 2, 3	0.1805, 0.3609, 0.4511
1	clean	-	5	5, 10, 14	1, 2, 3	0.0912, 0.1823, 0.2279
1	clean	-	10	5, 10, 14	1, 2, 3	0.0912, 0.1823, 0.2279
0.5	rough	-	5	5, 10, 14	1, 2, 3	0.1805, 0.3609, 0.4511
0.5	rough	-	10	5, 10, 14	1, 2, 3	0.1805, 0.3609, 0.4511
2	rough	-	5	5, 10, 14	1, 2, 3	0.0451, 0.0902, 0.1128
2	rough	-	10	5, 10, 14	1, 2, 3	0.0451, 0.0902, 0.1128
0.5	rough	VG1, VG2, VG3, VG4, VG5, VG6	5	5, 10, 14	1, 2, 3	0.1805, 0.3609, 0.4511
0.5	rough	VG1, VG2, VG3, VG4, VG5, VG6	10	5, 10, 14	1, 2, 3	0.1805, 0.3609, 0.4511
2	rough	VG1, VG2, VG3, VG4, VG5, VG6	5	5, 10, 14	1, 2, 3	0.0451, 0.0902, 0.1128
2	rough	VG1, VG2, VG3, VG4, VG5, VG6	10	5, 10, 14	1, 2, 3	0.0451, 0.0902, 0.1128

2.4. Instrumentation for data acquisition

The normal and tangential forces were calculated from surface pressures on the airfoil measured using a distribution of 102 pressure ports on the model, including 1 port on the blunt trailing edge. A traversable wake rake with 67 total pressure and 16 static pressure tubes was used to assess the total drag. The traverse mechanism is important to average over the spanwise periodic wake generated due to the presence of the VG arrays. Each traverse spanned a length of at least two pairs of VGs ($2D$, as illustrated in Figure 3a). The wake rake traverse motor was not as fast as the actuator motor for pitching at the higher amplitudes and frequencies. To maintain conformity in test conditions while comparing different test cases, the wake rake was not used in dynamic measurements. Drag was calculated only from the pressure measurements in this case.

2.5. Data processing and sources of uncertainty

The measured pressures were used to calculate the lift C_l and drag C_d on the airfoil. Drag can be calculated from the wake rake total pressure $C_{p,t}$ and static pressure $C_{p,s}$, as in Equation (3)[27]. Using the drag and the normal force C_n, the lift can be calculated for each angle of attack α as in Equation (5). These values are the uncorrected values represented with a $'$ symbol throughout the paper. Lift and drag values were corrected for solid and wake blockage using the Allen and Vincenti corrections [28], and for wake bouyancy and lift interference (streamline curvature) using the corrections from Garner et al. [29]. This correction procedure is standard and well-documented in literature [30] and thus left out of this paper due to the page limit. An example of the level of these corrections is presented in Figure 4. When the wake became unstable or wider than the wake rake, drag was calculated instead from the model pressures, as is common practice.

$$C'_d = \frac{2}{c}\int_{wake} \sqrt{C_{p,t} - C_{p,s}}\left(1 - \sqrt{C_{p,t}}\right) dy \tag{3}$$

$$C'_n = \int_0^1 \left(C_{p,l} - C_{p,u}\right) d\left(\frac{x}{c}\right) \tag{4}$$

$$C'_l = \frac{C'_n}{\cos(\alpha)} - C_d \cdot \tan(\alpha) \tag{5}$$

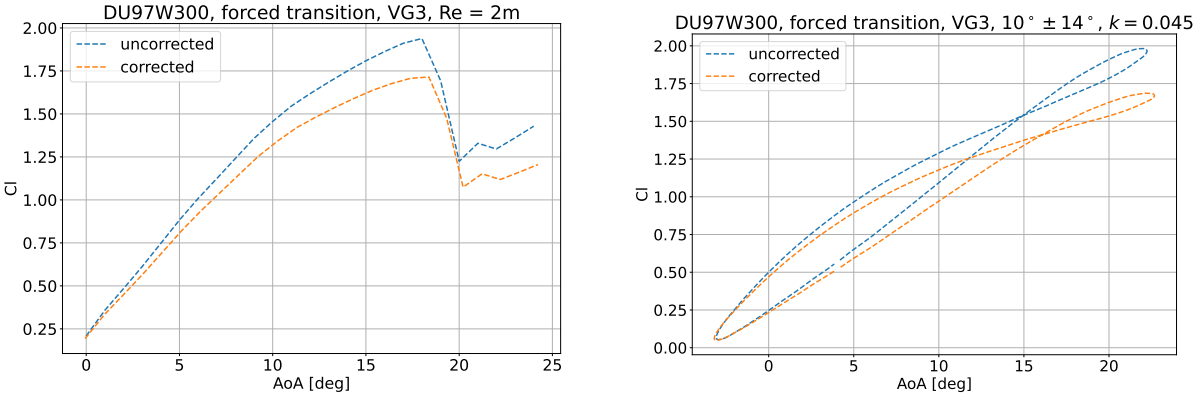

(a) Steady, forced transition, VG3

(b) Unsteady forced transition, VG3

Figure 4: Comparing the effect of wind tunnel corrections for steady and unsteady cases.

The unsteady pressures were measured for at least 150 cycles with a sampling rate of 300 Hz for each case. This ensured enough cycles to reach statistical stability in the surrounding flow field. The unsteady measurements were also corrected for the effects of the tubes connecting the pressure ports to the scanner. These tubes cause a phase lag and attenuation carried by the signal at the transducer compared to the signal at the surface of the airfoil. This is done using a user-friendly Matlab tool PreMeSys v2.0 based on the theory of Bergh and Tijdeman [31, 32] that defines a process to determine the response time of a measurement system consisting of pressure tubes and transducers connected in series. The pressure relationship for consecutive tubes and a series of N tubes is given respectively in Equations (6) and (7)

$$\frac{p_1}{p_0} = \left[\cosh(\varphi L) + \frac{V_v}{V_t}\left(\sigma + \frac{1}{k}\right) n\varphi L \sinh(\varphi L)\right]^{-1} \tag{6}$$

$$\frac{p_N}{p_0} = \frac{p_N}{p_{N-1}}\frac{p_{N-1}}{p_{N-2}}\cdots\frac{p_1}{p_0} \tag{7}$$

$$\text{with} \quad \varphi = \frac{v}{a_0}\sqrt{\frac{J_0\langle\alpha\rangle}{J_2\langle\alpha\rangle}}\sqrt{\frac{\gamma}{n}} \quad \text{and} \quad \alpha = i^{\frac{3}{2}} R\sqrt{\frac{\rho_s \nu}{\mu}} \tag{8}$$

where φ is the shear wave number including viscosity, i is the imaginary unit, ρ_s is the mean density, v is the frequency, μ is the absolute fluid viscosity, $n = \left[1 + \frac{\gamma-1}{\gamma}\sqrt{\frac{J_2\langle\alpha\rangle\sqrt{Pr}}{J_0\langle\alpha\rangle\sqrt{Pr}}}\right]^{-1}$ is the polytropic constant, $Pr = \frac{\mu C_p}{\lambda}$ is the Prandtl number, $\gamma = \frac{C_p}{C_v}$ is the specific heat ratio, J_m is the Bessel function of the first kind with order m, σ is the dimensionless increase in transducer volume due to diaphragm deflection, and k is the polytropic constant for the volumes. The tube geometry parameters are described by radius R and length L, while the transducer and tube volumes are V_v and V_t. The effect of a possibly oscillating air column in the pressure tubes due to the airfoil motion is not included in these corrections.

For the current setup, two sets of pressure tubes of diameter 1.8 mm (connected to the model pressure taps), and diameter 1 mm (connected to the pressure scanner) are used alongside adaptors of inner diameter 0.8 mm to connect both sets of tubes. The larger diameter tubes connected to the model are remnants of the fact that the airfoil model was first manufactured for compatibility with an older pressure measurement system that is no longer used in the TU Delft LTT. Both sets of tubes are 90 cm long and the adaptor is 1 cm long. An example of the corrected pressure signal is shown in Figure 5 for 5 cycles of pitching motion for the case of the airfoil with ZZ tape and VG3 pitching between $5° \pm 5°$ at 1 Hz.

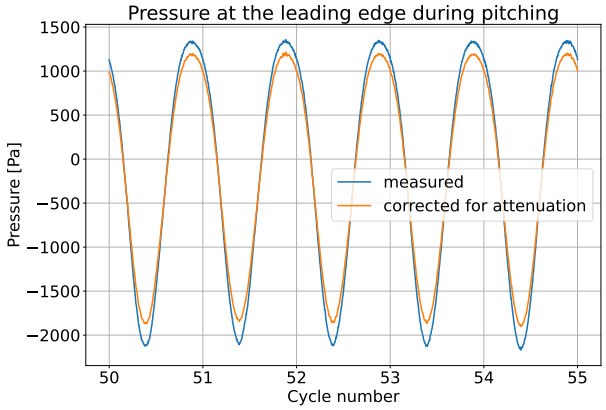

Figure 5: Comparing the measured and corrected pressure signal at the leading edge pressure channel for the airfoil with ZZ tape and VG3 pitching between $5° \pm 5°$ at 1 Hz.

3. Results and discussion

A selected number of cases from the wide range of measured cases are discussed in this paper to explore the impact of VGs on dynamic stall behaviour. For all cases, the goal is to explore how effectively different VGs mitigate the detrimental effects of leading edge roughness on the airfoil lift. Thus, every comparison includes the clean and rough cases, along with different VG cases. First, the static polars are explored under the lowest and highest Reynolds numbers tested to study the effectiveness of changing VG array parameters. In each case, the delay in the stall angle of attack and the maximum lift coefficient are used to compare the effectiveness of the VG array. While the polars extend to deep stall regions in some cases, this paper focuses on regular stall. The most effective VG array under static conditions (VG3) is chosen for the unsteady results to study how it impacts dynamic stall.

3.1. Static behaviour

The static measurements first establish a baseline with the clean and rough polars. Figure 6a shows a small effect of Reynolds number on the clean airfoil, while the effect of Reynolds number is much larger on the rough airfoil. On the clean airfoil, increasing Reynolds number brings faster stall onset at a lower angle of attack, with a minor reduction in $C_{l_{max}}$. As expected, applying roughness via the zigzag transition strip results in a significantly earlier stall onset and a significantly lower $C_{l_{max}}$ than a free transition airfoil. An earlier transition produces thicker boundary layers, a lower effective camber of the airfoil, and earlier flow separation. As seen in the relative loss of $C_{l_{max}}$ in Figure 6c, the sensitivity to forced transition increases up to a Reynolds number of 1 million, and decreases very slowly with Reynolds number thereafter. The behaviour after 1 million mirrors the earlier measured behaviour of this airfoil at higher Reynolds numbers from literature [23, 33]. The result for Reynolds number 0.5 million seems to be an outlier and can be attributed to a potentially insufficient tripping height, causing the transition to occur closer to the natural transition location than the forced transition location. This will be investigated in future work with the help of flow visualisation data acquired during the test campaign.

When VGs are applied (Figure 7), the effect of roughness is mitigated. The mitigation is much more significant for the higher Reynolds number than for the lower one. This is chalked up to the fact that at lower Reynolds numbers, roughness does not create as early of a stall onset or as large of a loss in $C_{l_{max}}$ as it does at higher Reynolds numbers. Figure 7a shows that VGs can significantly restore the loss of lift due to roughness, and larger VGs can even surpass the

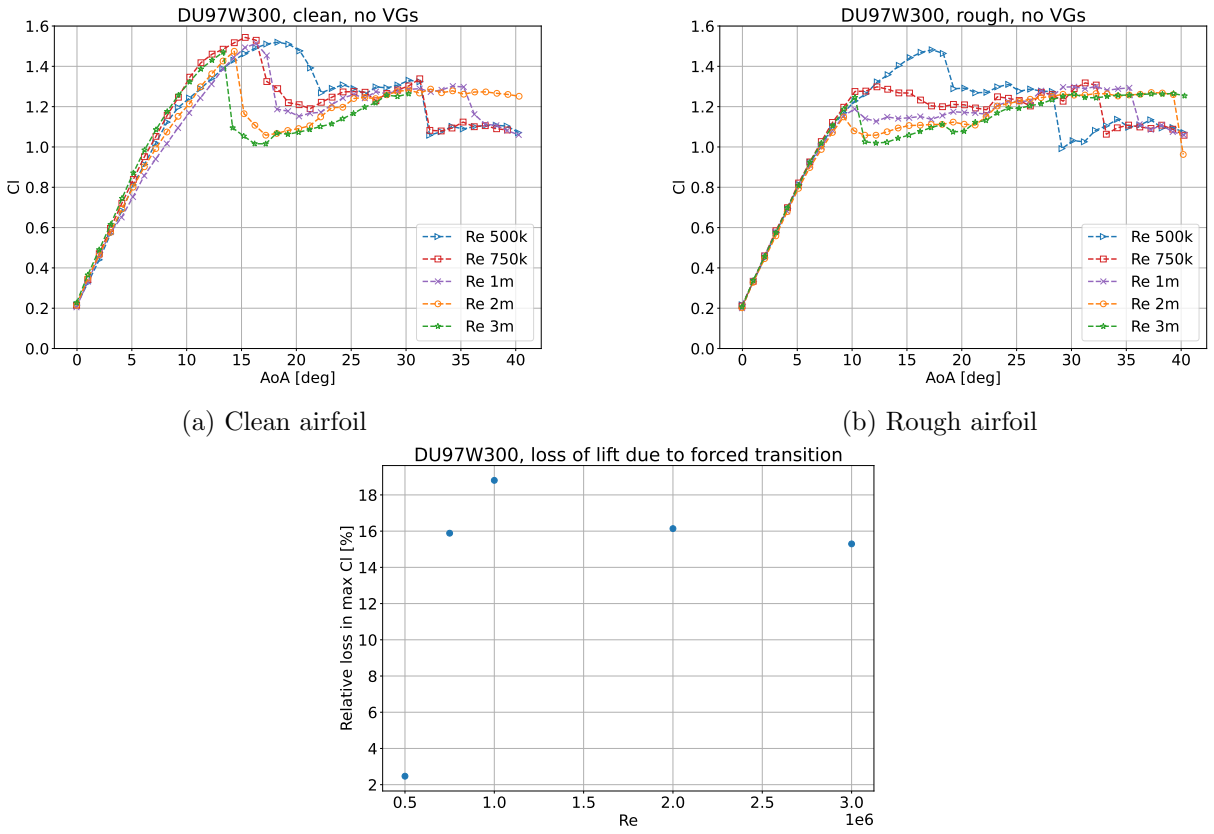

(a) Clean airfoil

(b) Rough airfoil

(c) Max Cl difference

Figure 6: Establishing a baseline for the clean and rough airfoil at different Reynolds numbers

lift produced by a clean airfoil. VG1 with $h/c \approx 1\%$ just about restores the rough airfoil to the lift levels of the clean airfoi, while VG3 with $h/c > 1\%$ increases the lift even beyond clean airfoil levels. VG2 with $h/c << 1\%$ restores some lift to the rough airfoil, but still falls behind the clean airfoil. Delaying stall, however, comes with a sharper drop in lift post-stall, as the post-stall lift of all three VGs is nearly identical. This is expected to impact the dynamic stall behaviour of the different VGs.

Keeping the vane size constant and varying the placement of the VGs has a secondary effect (Figure 7b). For example, bringing consecutive counter-rotating vanes closer while leaving larger gaps between consecutive pairs (i.e., VG5) seems to have a detrimental effect on the effectiveness of stall delay. This is expected because large parts of the airfoil remain free from the effect of the vortices and only a small part experiences the enhanced mixing that allows the flow to stay attached. Similarly, increasing the inclination angle of the vanes in VG6 also has a detrimental effect due to possible earlier interactions of neighbouring vortex pairs, decreasing the effectiveness of the mixing. Interestingly, rectangular vanes (VG4) perform slightly worse than triangular vanes (VG3), despite the expectation that a rectangular vane would keep the vortices closer to the surface, thus energising even lower parts of the boundary layer than a triangular vane. These observations will be further studied with flow visualisation to understand how different VG array parameters affect the vortices and their interaction with the separating boundary layer.

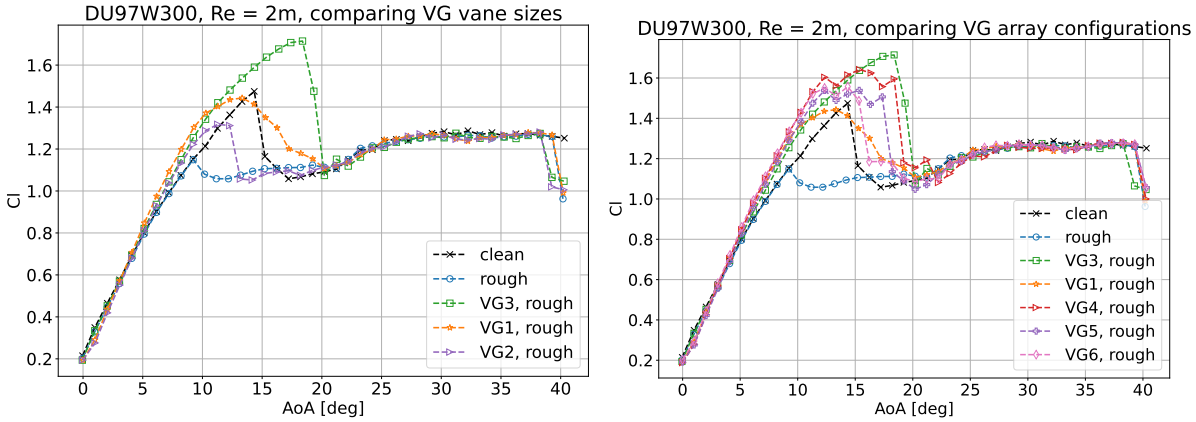

(a) Stall delay scales directly with the vane size (b) VG shape and placement have a secondary effect

Figure 7: Impact of VG geometry on the effectiveness of stall delay.

3.2. Dynamic Results

Dynamic stall behaviour of the clean, rough, and rough airfoil with VGs is presented in Figures 8 to 10. VG3 is used to demonstrate the effect of VGs because VG3 performs the best at delaying stall and increasing $C_{l_{max}}$ of all the VGs. When the airfoil is pitching within the static attached flow region (Figure 8), there is a hysteresis effect due to the airfoil motion. The unsteady lift is lower than static lift because the airfoil motion prevents the aerodynamic forces from reacting to the highest angle of attack before the airfoil has moved back to a lower angle. Increasing the reduced frequency further reduces the lift polar's slope and increases the difference between the lift in the upstroke and downstroke branches (i.e. the width of the loop) because this lag becomes larger. Thus, the lowest frequency produces the highest maximum unsteady lift. The VG case has the highest hysteresis effect, i.e., the gap between the upstroke and downstroke branches of the lift polar is the highest for the VG case.

When the airfoil is pitching in and out of the static separated flow (Figure 9) region, the aerodynamic forces can reach the maximum static lift. The stall vortex is released when the airfoil reaches the static stall angle of attack. However, the pitching motion keeps increasing the angle of attack while the stall vortex is rolling down the airfoil surface to the trailing edge. This keeps increasing the lift even beyond the static stall angle of attack. Before the stall vortex can reach the trailing edge of the airfoil, the pitching motion reduces the angle of attack back to attached region, preventing flow from fully separating from the airfoil surface. Thus, unsteady lift at static stalled angles is higher than steady lift. Higher pitching frequencies cause the airfoil to spend less time in the post-static stall angles and move back faster to static attached flow angles before the stall vortex rolls to the trailing edge. Thus, the higher frequencies produce a higher maximum lift. Reattachment occurs at a lower angle of attack for low frequency and at a higher angle of attack for higher frequency. The delay in stall and the increase in maximum lift is even higher in the rough case, although the difference between the upstroke and downstroke lift is also higher. Because of the stall delay due to VGs, the VG case still pitches mostly between static attached flow angles. Thus, the trend of the effects of increasing frequency is actually the opposite of the clean and rough airfoil. Similar to the previous pitching motion, the VG case higher frequencies bring wider hysteresis loops, unlike the clean and rough for these angle of attack and amplitude. The maximum unsteady lift of the VG case is still higher than the clean and rough case.

With large amplitudes, the airfoil is subject to pitching in and out of the static stall region of the VG case(Figure 10). Stall delay in the unsteady lift is observed. The clean and rough

configurations meanwhile are pitching deep into their respective static separated flow regions. The rough configuration reaches unsteady stall at these high angles of attack.

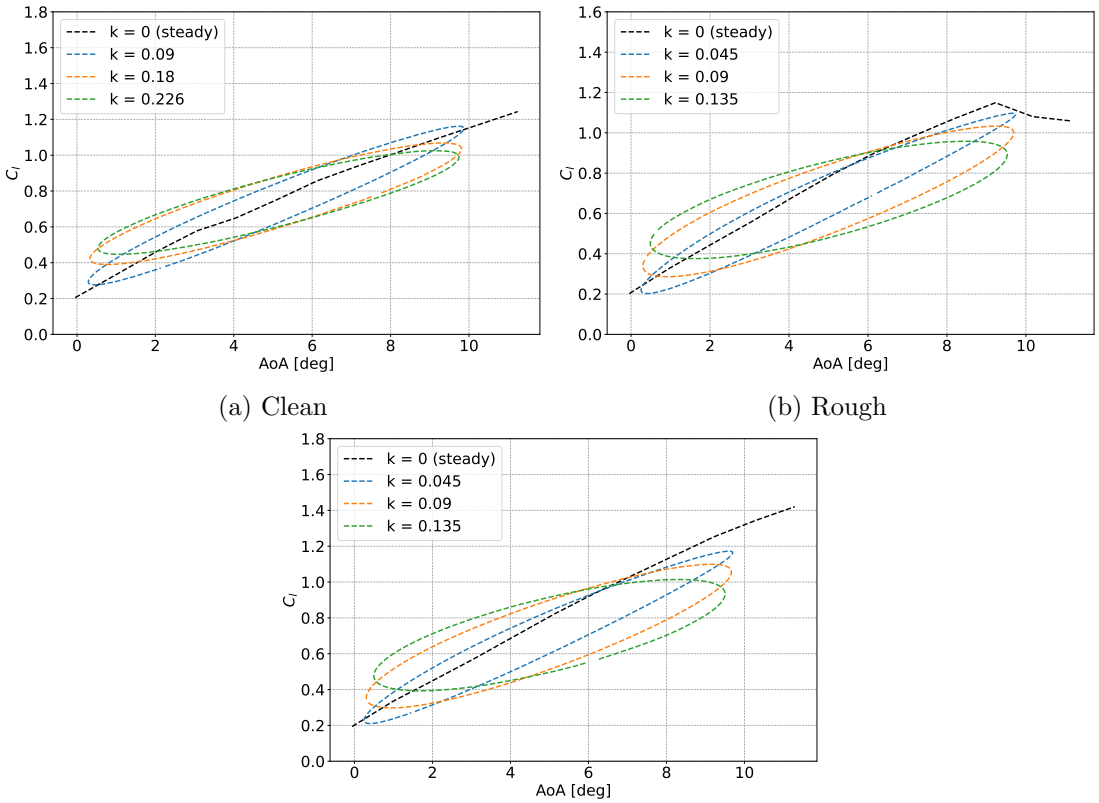

(a) Clean

(b) Rough

(c) Rough with largest VG (VG3)

Figure 8: Airfoil pitching entirely in the static attached flow region

4. Conclusions and Future Work

This experimental investigation, focusing on the dynamic stall behaviour of an airfoil with and without leading-edge roughness and vortex generators (VGs), has yielded novel insights into the performance of an inboard airfoil section. The static tests revealed the impact of the VG vane sizes and placement on delaying static stall. During dynamic stall, an airfoil with appropriately designed VGs experiences unsteady stall delayed till even higher angles of attack, producing a higher maximum unsteady lift. They also produce wider hysteresis loops compared to the airfoil without VGs. The flow visualisation of the airfoil boundary layer will be used in future work to understand the vortex-boundary layer interaction in the static stall and how the shed vortices may play a role in this behaviour of the aerodynamic forces in the dynamic stall.

Acknowledgement of funding

This work was carried out in conjunction with the VoGUe project funded by a Privaat-Publieke Samenwerkingen-toeslag (PPS toeslag) granted by the Netherlands Enterprise Agency (RVO). Partners involved in the VoGUe project are TNO, TU Delft, and Vestas Wind Systems A/S.

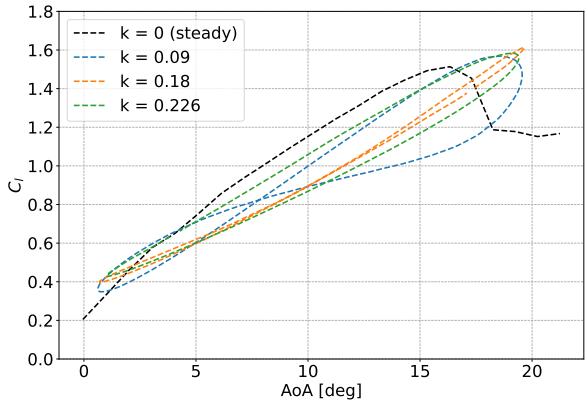

(a) Clean

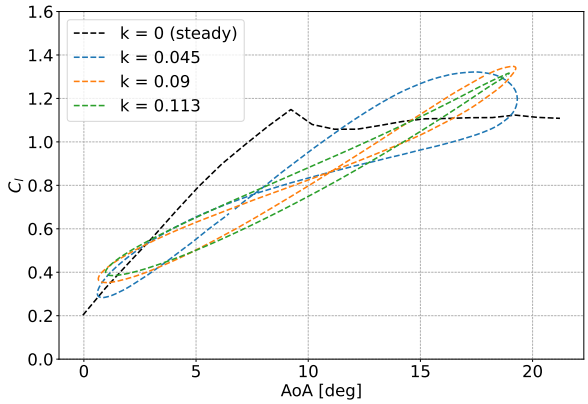

(b) Rough

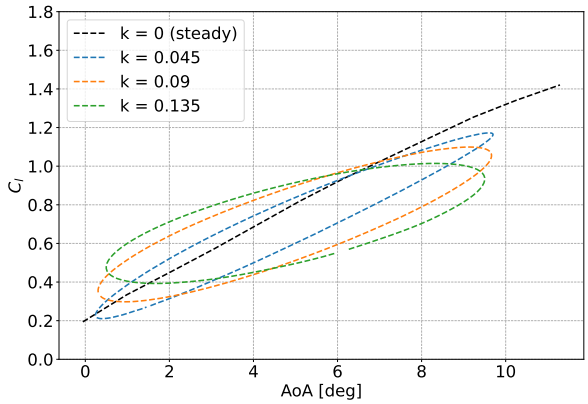

(c) Rough with largest VG (VG3)

Figure 9: Pitching in and out of static stall region

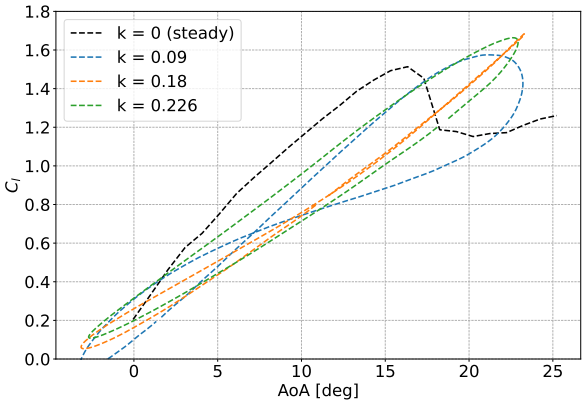

(a) Clean

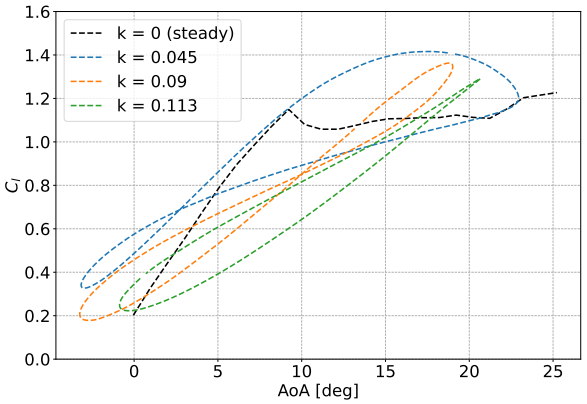

(b) Rough

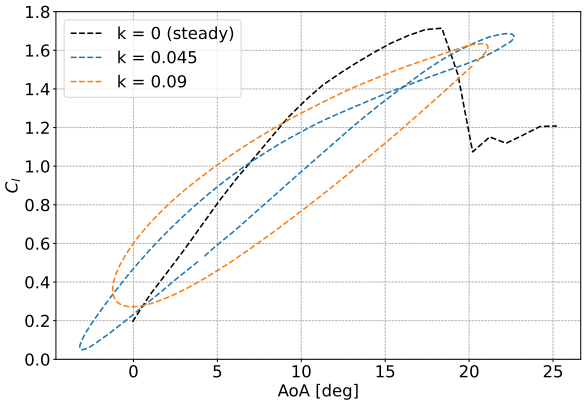

(c) Rough with largest VG (VG3)

Figure 10: Pitching deeper into the static stall region

References

[1] IRENA 2019 Future of wind: Deployment, investment, technology, grid integration and socio-economic aspects (A Global Energy Transformation paper) Tech. rep. International Renewable Energy Agency, Abu Dhabi

[2] Schepers J G, Ceyhan O, Savenije F J, Stettner M, Kooijman H J, Chaviarapoulos P, Sieros G, Simao Ferreira C S, Sørensen N, Wächter M, Stoevesandt B, Lutz T, Gonzalez A, Barakos G, Voutsinas A, Croce A and Madsen J 2015 *33rd Wind Energy Symposium* (American Institute of Aeronautics and Astronautics Inc.(AIAA)) pp 291–310

[3] McKenna R, Ostman P and Fichtner W 2016 *Renewable and Sustainable Energy Reviews* **53** 1212–1221

[4] Shipley D, Miller M, Robinson M, Luttges M and Simms D 1995 Techniques for the Determination of Local Dynamic Pressure and Angle of Attack on a Horizontal Axis Wind Turbine Tech. rep. National Renewable Energy Laboratory (NREL) Golden, CO (United States)

[5] Choudhry A, Arjomandi M and Kelso R 2013 *Proceedings of the Institution of Mechanical Engineers, Part A: Journal of Power and Energy* **227** 338–351

[6] Leishman J G 2002 *Wind Energy* **5** 85–132

[7] Rasmussen F, Petersen J and Madsen H 1998 *1998 ASME Wind Energy Symposium* (Reston, Virigina: American Institute of Aeronautics and Astronautics) pp 44–51

[8] Corke T C and Thomas F O 2015 *Annual Review of Fluid Mechanics* **47** 479–505

[9] Han W, Kim J and Kim B 2018 *Renewable Energy* **115** 817–823

[10] Herring R, Dyer K, Martin F and Ward C 2019 *Renewable and Sustainable Energy Reviews* **115** 109382

[11] Lin J C 2002 *Progress in Aerospace Sciences* **38** 389–420

[12] Griffin D A 1996 Investigation of Vortex Generators for Augmentation of Wind Turbine Power Performance

[13] Skrzypiński W, Gaunaa M and Bak C 2014 *Journal of Physics: Conference Series* **524**

[14] Ravishankara A K, Bakhmet I and Özdemir H 2020 *Journal of Physics: Conference Series* **1618** 52031

[15] Gutiérrez R, Llórente E, Echeverría F and Ragni D 2020 *Journal of Physics: Conference Series* **1618** 52058

[16] Baldacchino D, Ferreira C, Tavernier D D, Timmer W A and Van Bussel G J W 2018 *Wind Energy* **21** 745–765

[17] Lögdberg O, Fransson J H M and Alfredsson P H 2009 *Journal of Fluid Mechanics* **623** 27

[18] Godard G and Stanislas M 2006 *Aerospace Science and Technology* **10** 181–191

[19] Zhu C, Chen J, Wu J and Wang T 2019 *Energy* **189** 116272

[20] Zhu C, Qiu Y, Feng Y, Wang T and Li H 2022 *Energy Conversion and Management* **251** 115015

[21] Li S, Zhang L, Xu J, Yang K, Song J and Guo G 2020 *Journal of Renewable and Sustainable Energy* **12** 63304

[22] De Tavernier D, Ferreira C, Viré A, LeBlanc B and Bernardy S 2021 *Renewable Energy* **172** 1194–1211

[23] Timmer W A and van Rooij R P J O M 2003 *Journal of Solar Energy Engineering* **125** 488–496 ISSN 0199-6231

[24] Ashill P R, Fulker J L and Hackett K C 2005 *The Aeronautical Journal* **109** 205–232

[25] Gould D G 1956 The use of vortex generators to delay boundary layer separation: theoretical discussion supported by tests on a CF-100 aircraft Tech. rep. National Research Council of Canada. Division of Mechanical Engineering. National Aeronautical Establishment

[26] Carr L W 1988 *Journal of Aircraft* **25** 6–17

[27] Jones B 1936 The Measurement of Profile Drag by the Pitot-Traverse Method Tech. rep. The Cambridge University Aeronautics Laboratory (R&M No. 1688)

[28] Allen H J and Vincenti W G 1944 Wall interference in a two-dimensional-flow wind tunnel, with consideration of the effect of compressibility Tech. Rep. 782 NACA

[29] Garner H C, Rogers E W E, Acum W E A and Maskell E C 1966 Subsonic Wind Tunnel Wall Corrections Tech. rep. Advisory Group for Aerospace Research and Development (AGARD)

[30] Timmer W A 2021 *Handbook of Wind Energy Aerodynamics* (Cham: Springer International Publishing) pp 1–29

[31] Boerrigter H L 1996 *PreMeSys: A Simulation Program to Determine the Frequency and Time Response of a Pressure Measurement System* Technical memorandum (Von Karman Institute for Fluid Dynamics)

[32] Bergh H and Tijdeman H 1965 Theoretical and experimental results for the dynamic response of pressure measuring systems Tech. rep. Nationaal Lucht en Ruimtevaartlaboratorium

[33] Timmer W A and Schaffarczyk A P 2004 *Wind Energy* **7** 295–307 ISSN 1095-4244